Evaluation of a Strategy for the Assimilation of Satellite Radiance Observations with the Local Ensemble Transform Kalman Filter

José A. Aravéquia *

Centro de Previsão de Tempo e Estudos Climáticos,

São Paulo, Brazil

Istvan Szunyogh

Texas A&M University, College Station, TX, USA

Elana J. Fertig

John Hopkins University, Baltimore, MD, USA

Eugenia Kalnay and David Kuhl

University of Maryland, College Park, Maryland, USA

Eric J. Kostelich

Arizona State University, Tempe, Arizona, USA

ABSTRACT

This paper evaluates a strategy for the assimilation of satellite radiance observations with the Local Ensemble Transform Kalman Filter (LETKF) data assimilation scheme. The assimilation strategy includes a mechanism to select the radiance observations that are assimilated at a given grid point and an ensemble-based observation bias correction technique. Numerical experiments are carried out with a reduced (T62L28) resolution version of the model component of the National Centers for Environmental Prediction (NCEP) Global Forecast System (GFS). The observations used for the evaluation of the assimilation strategy are AMSU-A Level 1B brightness temperature data from the Earth Observing System (EOS) Aqua spacecraft. The assimilation of these observations, in addition to all operationally assimilated non-radiance observations, leads to a statistically significant improvement of both the temperature and wind analysis in the Southern Hemisphere. This result suggests that the LETKF, combined with the proposed data assimilation strategy for the assimilation of satellite radiance observations, can efficiently extract information from radiance observations.

* *Corresponding author address:* José A. Aravéquia, Centro de Previsão de Tempo e Estudos Climáticos, Rodovia Dutra, km 40, CEP 12630-000, Cachoeira Paulista, São Paulo, Brazil.

E-mail: araveq@cptec.inpe.br

1. Introduction

Although ensemble-based Kalman Filter data assimilation schemes were first proposed more than a decade ago (Evensen 1994; Burgers et al. 1998; Houtekamer and Mitchell 1998), evidence has emerged only recently that ensemble-based Kalman filters may be viable alternatives to the variational techniques in operational numerical weather prediction. In particular, several research groups have designed computationally efficient ensemble-based Kalman filters that have been successfully tested with observations of the real atmosphere in both global (e.g. Houtekamer et al. 2005; Whitaker et al. 2004, 2008; Szunyogh et al. 2008; Miyoshi and Sato 2007; Miyoshi and Yamane 2007) and limited-area (e.g. Torn and Hakim 2008; Bonavita et al. 2008) settings.

In this paper, we focus on the performance of one particular ensemble-based Kalman filter scheme, the Local Ensemble Transform Kalman Filter (LETKF), for assimilating satellite radiance observations. The LETKF algorithm was developed by Ott et al. (2004) and Hunt et al. (2004, 2007) and was tested on both simulated observations in the perfect model scenario (Szunyogh et al. 2005) and on observations of the real atmosphere (Miyoshi and Sato 2007; Szunyogh et al. 2008; Whitaker et al. 2008). In particular, Szunyogh et al. (2008) and Whitaker et al. (2008) assimilated non-radiance observations in a reduced-resolution version of the model component of the NCEP GFS and found that the performance of the LETKF was superior to that of the Statistical Spectral Interpolation (SSI) of NCEP in data-sparse regions.[1]

Our goal here is to extend the study of Szunyogh et al. (2008) by augmenting the observa-

[1]The SSI was the operational 3D-Var data assimilation system of NCEP until April 2007.

tional data set with satellite radiance observations. To assimilate these satellite observations, we employ techniques for the localization and bias correction of the satellite radiance observations, which we developed and tested in an idealized setting in Fertig et al. (2007, 2009). The observations we assimilate are AMSU-A Level 1B brightness temperature data from an instrument flown on the Earth Observing System (EOS) Aqua spacecraft (Olsen 2007). Hereafter, we refer to brightness temperature and radiance observations collectively as radiance observations, as the assimilation of both of these types of data requires the use of a radiative transfer model. The performance of the LETKF in assimilating radiance observations is assessed by comparing the results to those obtained by assimilating only the non-radiance observations.

The structure of the paper is as follows. Section 2 provides a summary of our implementation of the LETKF on the model component of the NCEP GFS, while Section 3 is a brief description of the AMSU-A observational data sets. Section 4 explains the design of our numerical experiments, whose results are reported in section 5. Section 6 offers a summary of our conclusions.

2. The LETKF for the NCEP GFS model

In what follows, we explain our implementation of the LETKF algorithm on the model component of the NCEP GFS. We introduce the major components of the data assimilation algorithm and summarize the data assimilation procedure for the conventional non-radiance observations. Finally, we explain the modifications required to assimilate satellite radiance observations.

a. Definitions

We assume that, similar to the practice of operational numerical weather prediction, observations are assimilated from the observation time window

$$\tau_n = [t_n - \Delta t/2, t_n + \Delta t/2]$$

at the analysis time t_n. The observations from τ_n form the vector of observations $\mathbf{y}_n^o$. We introduce the notation $\boldsymbol{\gamma}_n$ for the state space trajectory of the model in τ_n, that is,

$$\boldsymbol{\gamma}_n = \mathbf{x}(t), \qquad t \in \tau_n, \tag{1}$$

where the vector $\mathbf{x}(t)$ is the finite-dimensional representation of the atmospheric state on the model grid. The two inputs of the LETKF algorithm are the observation vector $\mathbf{y}_n^o$ and an ensemble of K analyses $\mathbf{x}_{n-1}^{a(k)}$, $k = 1, 2, \ldots, K$, from the previous analysis time $t_{n-1} = t_n - \Delta t$.

The LETKF consists of a forecast step and a state-update step. In the forecast step, each ensemble member is integrated forward by the time interval $\frac{3}{2}\Delta t$ using the K members of the analysis ensemble $\mathbf{x}_{n-1}^{a(k)}$, $k = 1, \ldots, K$, as initial conditions to obtain an ensemble of background forecast trajectories, $\boldsymbol{\gamma}_n^{b(k)}$, $k = 1, \ldots, K$. In our current implementation of the LETKF, the members of the background ensemble are 6-hour forecast trajectories starting at the 3-hour forecast lead time and ending at the 9-hour forecast lead time relative to t_{n-1}.

The formulation of the state update step of the LETKF, similar to that of all other modern data assimilation schemes, is based on the assumption that we know the observation operator $\mathbf{h}(\boldsymbol{\gamma}_n)$ that satisfies

$$\mathbf{y}_n^o = \mathbf{h}(\boldsymbol{\gamma}_n^t) + \boldsymbol{\varepsilon}_n, \quad t \in \tau_n. \tag{2}$$

Here, $\boldsymbol{\gamma}_n^{\boldsymbol{t}}$ is the model representation of the (unknown) true system trajectory and $\boldsymbol{\varepsilon}_n$ is a vector of Gaussian random observation noise with zero mean and error covariance matrix $\mathbf{R}_n$. In practice, the observation operator typically consists of an interpolation of $\boldsymbol{\gamma}_n$ to the time and location of the observations and a conversion of the model variables to the observed quantities. In our implementation of the LETKF on the NCEP GFS, the time interpolation component of $\mathbf{h}(\boldsymbol{\gamma}_n)$ for all types of the observations is performed by storing the background trajectories $\boldsymbol{\gamma}_n^{b(k)}$, $k = 1, \ldots, K$, with a 1-hour resolution and applying a linear interpolation to the stored model fields to obtain the ensemble of model states at the observation time with a one minute accuracy.

In what follows, we discuss how to obtain an analysis $\mathbf{x}_n^a$ at time t_n and drop the subscript n. The LETKF obtains the vector components of the analysis $\mathbf{x}^a$ independently for each grid point. We define a local state vector $\mathbf{x}_\ell$ that is composed of the model variables at model grid point ℓ. The LETKF generates a K-member ensemble of local analyses, $\mathbf{x}_\ell^{a(k)}$, $k = 1, \ldots, K$ by computing an ensemble of "weight vectors" $\mathbf{w}^{a(i)}$, $k = 1, \ldots, K$ such that

$$\mathbf{x}_\ell^{a(k)} = \overline{\mathbf{x}}_\ell^b + \mathbf{X}_\ell^b \mathbf{w}_\ell^{a(k)}. \tag{3}$$

Here $\overline{\mathbf{x}}_\ell^b$ is the ensemble mean of the local background state vectors $\mathbf{x}_\ell^{b(k)}$, $k = 1, \ldots, K$, and $\mathbf{X}_\ell^b$ is the matrix of background ensemble perturbations whose kth column is the kth background ensemble perturbation $\mathbf{x}^{b(k)} - \overline{\mathbf{x}}^b$. (The overbar indicates the ensemble mean.) The best estimate of the state at location ℓ is the mean of the analysis ensemble,

$$\overline{\mathbf{x}}_\ell^a = \overline{\mathbf{x}}_\ell^b + \mathbf{X}_\ell^b \overline{\mathbf{w}}_\ell^a. \tag{4}$$

The members of the global analysis ensemble, $\mathbf{x}^{a(k)}$, and the global analysis, $\mathbf{x}^a$, are obtained by collecting the local analyses, $\mathbf{x}_\ell^{a(k)}$ and $\overline{\mathbf{x}}_\ell^a$, for all locations ℓ.

b. Conventional observations

For the conventional (non-radiance) observations, we compute the weight vectors $\mathbf{w}_\ell^{a(k)}$, $k = 1, \ldots, K$, and their ensemble mean, $\overline{\mathbf{w}}_\ell^a$, by the following procedure:

0. The observation operator $\mathbf{h}(\boldsymbol{\gamma}_n)$ is defined. In the two horizontal spatial dimensions, $\mathbf{h}(\boldsymbol{\gamma}_n)$ is a simple bilinear interpolation. Since the vertical coordinate in the NCEP GFS model is σ (defined by the ratio of the pressure and the surface pressure) and the vertical position of the observations is given in pressure, the vertical interpolation for a given observation is carried out in three steps:

   (a) We calculate the pressure at each σ-level at the horizontal location of the observation by multiplying σ by the background surface pressure interpolated to the observational location.

   (b) We define 28 σ layers, each bounded by a pair of σ levels (the lowest layer is defined by the model surface and the lowest σ level).

   (c) We find the σ layer that contains the observation and linearly interpolate the logarithm of the pressure to the observation location using the pressure values at the two σ-levels that bound the layer.

1. The observation operator $\mathbf{h}(\boldsymbol{\gamma}_n)$ is applied to each member $\boldsymbol{\gamma}_n^{b(k)}$, $k = 1, 2, \ldots, K$, of the ensemble of background trajectories to obtain an ensemble $\mathbf{y}^{b(k)}$, $k = 1, \ldots, K$, of the model-predicted values of the observables at the observation locations. The ensemble average $\overline{\mathbf{y}}^b$ of the ensemble $\mathbf{y}^{b(k)}$, $k = 1, \ldots, K$, is computed and the matrix $\mathbf{Y}^b$ is constructed by taking its columns to be the vectors obtained by subtracting $\overline{\mathbf{y}}^b$ from

each ensemble member $\mathbf{y}^{b(k)}$, $k = 1, \ldots, K$.

2. The localization is performed. For each location (grid point) ℓ, the observations that are thought to have useful information about the atmospheric state at grid point ℓ are selected for assimilation. The selected observations form the local observation vector $\mathbf{y}_\ell^o$. The vector $\overline{\mathbf{y}}_\ell^b$ and the matrices $\mathbf{Y}_\ell^b$ and $\mathbf{R}_\ell$ are formed by selecting those vector components and matrix elements that are associated with the selected set of observations at ℓ. In the present study, we choose the localization parameters as follows:

   (a) In the horizontal direction, observations are considered from an 800-km radius neighborhood of the location (grid point) ℓ. The influence of observations is tapered as a function of the radius r from the grid point. In particular, $\mathbf{R}_\ell^{-1}$ is mulitplied by a factor $\mu(r)$ such that $\mu(r) = 1$ for $r \leq 500$ km and $\mu(r) = (800 - r)/300$ for 500 km $\leq r \leq$ 800 km.

   (b) In the vertical direction, observations are considered from a layer around ℓ. The depth of the layer is 0.35 scale height between model levels 1 and 15 (below $\sigma = 0.372$), and, starting with level 15, the depth gradually increases with height to reach 2 scale heights at the top of the model atmosphere (defined by $\sigma = 0.003$). (The scale height is defined by the vertical distance in which the surface pressure drops by a factor of $e \approx 2.718$.) Surface pressure observations are also considered from the local horizontal region when the state is analyzed at a model grid point, which is at or below model level 15.

   (c) The surface pressure components of the state vector are treated differently from

the other components. To obtain the surface pressure analysis at a location ℓ, we use all surface pressure observations from an 800 km radius of ℓ and all temperature and wind observations from a 800 km radius of ℓ between model levels 2 ($\sigma = 0.982$) and 5 ($\sigma = 0.916$). As for all other observation types, the influence of the surface observation is tapered beyond 500 km radius.

3. The weight vector $\overline{\mathbf{w}}_\ell^a$ is computed by

$$\overline{\mathbf{w}}_\ell^a = \tilde{\mathbf{P}}_\ell^a (\mathbf{Y}_\ell^b)^T \mathbf{R}_\ell^{-1} (\mathbf{y}_\ell^o - \mathbf{y}_\ell^b). \tag{5}$$

Here,

$$\tilde{\mathbf{P}}_\ell^a = [(k-1)\mathbf{I}/\rho + (\mathbf{Y}_\ell^b)^T \mathbf{R}_\ell^{-1} \mathbf{Y}_\ell^b]^{-1}, \tag{6}$$

where $\rho \geq 1$ is a multiplicative covariance inflation factor and $\mathbf{I}$ is the identity matrix. In our implementation, ρ is a smoothly varying three-dimensional scalar field: ρ tapers from 1.25 at the surface to 1.2 at the top of the model atmosphere in the SH extratropics and from 1.35 to 1.25 in the NH extratropics, while ρ changes smoothly throughout the tropics (between 25° S and 25° N) from the values of the SH extratropics to the values of the NH extratropics.

4. The matrix $\mathbf{W}_\ell^a = [(k-1)\tilde{\mathbf{P}}_\ell^a]^{1/2}$ is computed.

5. The weight vector $\overline{\mathbf{w}}_\ell^a$ is added to each row of $\mathbf{W}_\ell^a$. The columns of the resulting matrix are the members of the ensemble of weight vectors $\mathbf{w}_\ell^{a(k)}$, $k = 1, \ldots, K$.

1) Satellite Radiance Observations

The assimilation procedure is more complicated for the radiance observations than for the conventional observations. The primary source of the added complexity is the observation operator $\mathbf{h}$, which, instead of the simple interpolation procedure described in step 0 of the LETKF algorithm, is the Community Radiative Transfer Model (CRTM Han et al. 2005) of the Joint Center for Satellite Data Assimilation (JCSDA).

One important issue is the bias in the observations: because the radiative transfer model is subject to large bias, in contrast to the case of the conventional observations, we cannot assume that the CRTM satisfies Eq. (2). We assume that the equality can be restored by adding a bias correction term $\mathbf{b}$ to the the output of the CRTM. That is, we assume that the bias corrected observation operator

$$\widehat{\mathbf{h}}(\boldsymbol{\gamma}, \boldsymbol{\beta}) = \mathbf{h}(\boldsymbol{\gamma}) + \mathbf{b} \tag{7}$$

satisfies the relation

$$\widehat{\mathbf{y}}^o = \widehat{\mathbf{h}}(\boldsymbol{\gamma}^{\boldsymbol{t}}) + \boldsymbol{\varepsilon}, \tag{8}$$

which is the analogue of Eq. (2). The dimension of the vectors $\widehat{\mathbf{h}}$, $\widehat{\mathbf{y}}^o$, and $\mathbf{b}$, which we denote by J, equals the total number of satellite channels for which observations are assimilated. The vector $\widehat{\mathbf{y}}^o$ is composed of the radiance components of $\mathbf{y}^o$, while the vector of bias correction parameters $\boldsymbol{\beta}$ is defined the following way: each component b_j of the bias correction vector $\mathbf{b}$ is estimated by the linear combination

$$b_j = \beta_j^0 + \sum_{i=1}^{I} \beta_j^i p_i, \qquad j = 1, \ldots, J, \tag{9}$$

of a set of "predictors" $p^i(t)$, $i = 1, \ldots, n$. The predictors can be chosen to be any scalar

parameters that can be determined from the model or from information provided with the observations (e.g. Eyre 1992; Derber and Wu 1998; Harris and Kelly 2001). Typical examples for model-based predictors are the skin temperature and the thickness of different atmospheric layers, while an example for an observation-related predictor is the scan angle at which the radiance observation is taken by the satellite-based observing instrument. In our formulation, the set of predictors is the same for all observations that form $\widehat{\mathbf{y}}^o$, but the coefficients $\beta_j^i(t)$, $i = 0, \ldots, I$, are different for the different channels and different instruments. Thus, the total number of bias correction coefficients is $M = (I + 1) \times J$. Since $b_j = \beta_j^0$ when all predictors are zero, we call β_j^0 the *intercept* for the channel associated with the jth component of the bias correction vector $\mathbf{b}$.

We obtain estimates of the bias parameters by the method of state augmentation (e.g. Friedland 1969; Derber and Wu 1998; Dee 2005): we augment the state vector $\mathbf{x}$ by the vector $\boldsymbol{\beta}$ of $(I + 1) \times J$ bias parameters to define the augmented state vector

$$\mathbf{z} = \begin{bmatrix} \mathbf{x} \\ \\ \boldsymbol{\beta} \end{bmatrix} \tag{10}$$

and obtain an estimate of the augmented state vector by applying the LETKF algorithm to the augmented state vector $\mathbf{z}$ instead of the state vector $\mathbf{x}$.

The bias components $\boldsymbol{\beta}^{b(k)}$, $k = 1, \ldots, K$ of the background ensemble members at t_n are assumed to be equal to the analyzed values $\boldsymbol{\beta}^{a(k)}$, $k = 1, \ldots, K$, of the bias parameters at the previous analysis time t_{n-1}. This is formally equivalent to assuming that the time evolution of the bias parameters is persistence, that is,

$$\boldsymbol{\beta}_n^{b(k)} = \boldsymbol{\beta}_{n-1}^{a(k)}, \qquad k = 1, \ldots, K. \tag{11}$$

The second important issue is the nonlocal nature of the observation operator for radiance: in contrast to the case of the conventional observations, where the observation operator for a given observation depends on the model state only at the nearby grid points, the output of the CRTM depends on the entire atmospheric column of the model atmosphere at the horizontal location of the observation. This suggests that the vertical component of the localization strategy, implemented in step 2 of the LETKF, must be modified for the radiance observations. Our modified data selection strategy is based on the vertical weighting function, w_l, which is computed by the CRTM for each radiance observation at all model levels $l = 1, \ldots, L$. To be precise, for a given observation, the CRTM computes the radiance by

$$h(\mathbf{x}) = R_s + \sum_{l=1}^{L} B(T_l) w_l, \tag{12}$$

where R_s is the contribution of the Earth's surface to the radiance, $T(l)$ is the temperature at model level l, L is the number of model levels, $B(T_l)$ is the Planck function, and the weights w_l, $l = 1, \ldots, L$, satisfy the condition

$$\sum_{l=1}^{L} B(T_l) w_l = 1. \tag{13}$$

We apply the cutoff-based observation strategy suggested by Fertig et al. (2007) to select the model levels where a given observation is assimilated, as follows:

- choose a cutoff parameter η $(0 < \eta \leq 1)$;
- find the model level $l^k_{\max}$, for each ensemble member $k = 1, \ldots, K$, at which w^k_l takes its maximum value $w^k_{\max}$;
- search for the bottom and the top of the deepest layer around level $l^k_{\max}$, in which the

weighting function satisfies the condition $w_l^k \leq \eta w_{\max}^k$;

- compute the ensemble mean, l_{top}, of the index of the top of the layer identified in the previous step and the ensemble mean, l_{bottom}, of the index of the bottom of the same layer;

- assimilate observations from the layers bounded by l_{bottom} and l_{top}.

A suitable value of η, which provides an analysis of acceptable accuracy at minimum computational cost, is found by numerical experimentation.

To incorporate the bias estimation procedure and data selection strategy we describe here, we make the following specific changes in the main steps of the LETKF algorithm:

0. The observation operator for the radiance observations is defined by $\widehat{\mathbf{h}}$.

1. The ensemble of radiance values at the observation locations, $\widehat{\mathbf{y}}^{b(k)}$, $k = 1, \ldots, K$, is obtained by applying $\widehat{\mathbf{h}}$ to the background trajectories $\boldsymbol{\gamma}^{b(k)}$, $k = 1, \ldots, K$.

2. The radiance observations that form the $\widehat{\mathbf{y}}_\ell^o$ component of $\mathbf{y}_\ell^o$ at the different grid points ℓ are selected for assimilation by the cutoff-based strategy.

Steps 3–5 of the algorithm, which provide the weights $\mathbf{w}_l^{a(k)}$ for the computation of the analysis of the local augmented state vector

$$\mathbf{z}_\ell^{a(k)} = \mathbf{z}_\ell^b + \mathbf{Z}_\ell^b \mathbf{w}_\ell^{a(k)}, \tag{14}$$

are the same as for the conventional observations. The state analysis components $\mathbf{x}^{a(k)}$ of $\mathbf{z}^{a(k)}$, $k = 1, \ldots, K$, are obtained as before, collecting the state vector components $\mathbf{x}_\ell^{a(k)}$ of the local analyses of the augmented state vectors $\mathbf{z}_\ell^{a(k)}$ for all locations ℓ. A different

procedure is needed, however, to obtain the global analysis ensemble of bias parameters, $\boldsymbol{\beta}^{a(k)}$, $k = 1, \ldots, K$, from the bias components $\boldsymbol{\beta}_\ell^{a(k)}$ of $\mathbf{z}_\ell^{a(k)}$, $k = 1, \ldots, K$. Because the bias component of the augmented state vector is composed of bias correction parameters for all satellite channels assimilated at location ℓ, the same bias parameter is estimated at many different locations ℓ. To obtain a single estimate of each of the M bias parameters, we average the local estimates of the bias parameters over all locations ℓ by the formula

$$\beta_m^{a(k)} = \frac{\sum_\ell \cos(\phi_\ell) \beta_{m,\ell}^{a(k)} \sigma_{m,\ell}^{-2}}{\sum_\ell \cos(\phi_\ell) \sigma_{m,\ell}^{-2}}, \qquad m = 1, \ldots, M. \tag{15}$$

Here, $\beta_m^{a(k)}$ and $\beta_{m,\ell}^{a(k)}$ are the mth components of $\boldsymbol{\beta}^{a(k)}$ and $\boldsymbol{\beta}_\ell^{a(k)}$, respectively, ϕ_ℓ is the latitude at location ℓ, and the factor $\cos(\phi_\ell)$ accounts for the dependence on the latitude of the area represented by a grid point. The factor $\sigma_{m,\ell}^{-2}$ is the inverse of the variance

$$\sigma_{m,\ell}^2 = (K-1)^{-1} \sum_{k=1}^{K} \left(\beta_{m,\ell}^{a(k)} - \beta_m^{a(k)} \right) \tag{16}$$

of the analysis ensemble for the mth component of the bias parameter vector $\boldsymbol{\beta}$ at location ℓ. Weighting with the inverse of the variance ensures that locations where the uncertainty in the estimate of a given bias parameter is larger contribute with a smaller weight to the global estimate of that bias parameter.

3. The Observations

Following the convention of operational numerical weather prediction for global models, we use a 6-hour window and prepare analyses four times a day, at 0000 UTC, 0600 UTC, 1200 UTC, and 1800 UTC. A typical example for the number of observations we assimilate is shown in Table 2. On any given day, we assimilate about 1 million observations, of which

about 15–20% are radiance observations. These radiance observations fill important data voids in the coverage by the conventional data (see Figures 1 and 2). We process many more observations than indicated by Table 2, but the number of observations is reduced by selecting only a subset of the radiance observations for assimilation and by rejecting observations that do not pass quality control. The data selection strategy and the quality control procedure are explained in Section 4.

a. Conventional Observations

We assimilate all conventional observations that were assimilated operationally at NCEP between January 1, 2004, 0000 UTC and February 29, 2004, 1800 UTC. This data set includes observations of the surface pressure by synoptic land stations; virtual temperature and surface pressure by surface marine observing platforms; splash-level virtual temperature by dropsondes; virtual temperature and wind by rawinsondes; sensible temperature and wind by commercial airliners; flight-level virtual temperature and wind by reconnaissance planes; cloud-drift wind by the GMS-5, METEOSAT-5, METEOSAT-7, GOES-8, and GOES-10; and QUICKSCAT surface wind by scatterometers. Figure 1 shows the spatial distribution of the assimilated temperature observations for a typical 6-hour observations time window.

b. AMSU-A Level 1B Brightness Temperature Data

The acronym AMSU stands for Advanced Microwave Sounding Unit. AMSU-A is primarily a temperature sounder that provides atmospheric information in the presence of non-precipitating clouds. We assimilate a subset of the AMSU-A Level 1B brightness temperature

data set, which contains calibrated and geolocated brightness temperatures in degrees Kelvin for 15 microwave channels. We assimilate only 8 of the 15 channels, since the observations from channels 1, 2, 3, and 15 have a strong surface signal component, while channels 12, 13, and 14 are strongly influenced by the atmospheric conditions at altitudes that are higher than the top of our model atmosphere. Figure 2 shows the spatial distribution of the assimilated AMSU-A observations for a typical 6-hour observations time window.

4. Numerical Experiments

The primary goal of our numerical experiments is to determine how much improvement is achieved in the analyses when, in addition to the conventional observations, we assimilate the AMSU-A observations with the proposed strategy. We assess the performance of the data assimilation system when the AMSU-A observations are included by comparing the analysis and short-term (48-h) forecast errors with those from two reference experiments. In one of these reference experiments, we assimilate the AMSU-A observations but do not apply bias correction to the radiance observations, while in the other reference experiment, we assimilate only the conventional observations.

a. Experiment design

In the two experiments that assimilate radiance observations, we do not assimilate more than one radiance observation per channel at a given grid point. Instead, we assimilate the first observation from the data set that satisfies all quality control criteria. In particular,

we do not assimilate observations from mixed-surface footprints (e.g., from areas where sea water is mixed with ice) and observations for which the scan angle is larger than 35 degree. We also reject observations for which the difference between the observed value and $\widehat{\mathbf{h}}(\mathbf{x})$ is more than five times larger than both the ensemble spread (standard deviation of the ensemble) and the presumed standard error of the observations.

The model used in this study is the 2004 model component of the operational NCEP GSF truncated to T62L28 resolution. This model is identical to the one that was used in Szunyogh et al. (2008) and Whitaker et al. (2008). The only important improvement in our LETKF data assimilation system, compared to the one we evaluated in Szunyogh et al. (2008), is the correction of a coding error that led to the rejection of most scatterometer observations in the former implementation of the system. This correction leads to an improvement of the analyses and short-term forecasts in the Southern Hemisphere extratropics near the surface. We use this improved set of analyses as the baseline for the evaluation of the results obtained with the augmented obsrvational data set. Despite the aforementioned coding error, the former version of the LETKF provided analyses and short-term forecasts that in the SH were, on average, more accurate at the 99% significance level than those obtained with the then-operational Spectral Statistical Interpolation (SSI) of NCEP. Consequently, our baseline data set consists of reasonably high quality analyses. We emphasize, however, that based on the information available to us, it is impossible to infer how the performance of the LETKF would compare to the SSI or the currently operational Grid-point Statistical Interpolation (GSI) of NCEP (Wu et al. 2002) in assimilating the satellite radiance observations we consider here.

b. Verification methods

We use the verification and significance test methods described in detail in Szunyogh et al. (2008). In particular, verification of the analyses and the 48-hour forecasts is made against the high-resolution (T254L64) operational real-time analyses of NCEP from 2004. While the statistical significance of the difference between the state estimation (analysis or forecast) errors with the proposed assimilation strategy and in the reference experiments is tested using a two-sample t-test (Wilks 2006). Our implementation of the test returns the probability with which the null hypothesis, i.e., that the difference between the time mean of the error statistics is the result of random statistical fluctuations, can be rejected. In our verification statistics, the time averaging is applied either to the root-mean-square error computed over a large domain in model grid space or to errors at model grid points.

c. LETKF parameters

Most of our choices of the LETKF parameters, which define the localization for the conventional observations and the variance inflation for the state vector components, are discussed in section 2. The radiance observations are corrected using two predictors: the skin temperature (p_1) and the scan angle (p_2), that is, the bias correction term is estimated by

$$b_j = \beta_j^0 + \beta_j^1 p_1 + \beta_j^2 p_2, \qquad j = 1, \ldots, J = 8. \tag{17}$$

Since the number of bias parameters is $I + 1 = 3$, the number of bias parameters that we estimate is $M = (I + 1) \times J = 24$. The global values of the bias correction parameters

are obtained from the local values by averaging them over all observation locations in three zonal latitude bands (90°S–30°S, 30°S–30°N, 30°N–90°N) using Equations (15) and (16).

We chose these particular predictors and averaging regions after testing the sensitivity of the results to the selection of these parameters by numerical experimentation. To be specific, we first added one or two predictors representing the depth of selected pressure layers of the atmosphere. (Such predictors are often used by the NWP centers and we hoped that we could define a single global value of each bias parameter in a similar way.) The accuracy of the analyses and ensuing forecasts, however, was clearly degraded by adding the extra predictors. We observed similar degradations when we averaged the local estimates of the bias parameters over five latitude bands, instead of three, breaking up the both extratropical averaging regions into midlatitude and polar regions. In another series of experiments, we reduced either the number of predictors or the number of averaging regions and found that those configurations performed similarly well to our standard choice of two predictors (three bias parameters) and three averaging regions. The only disadvantage of these configurations was that anomalously large, though non-catastrophic, errors occurred either in the Tropics or in one of the polar regions at a few analysis times.

We find that a 60-member ensemble provides a sufficiently large number of degrees of freedom to obtain accurate estimates of the bias parameters and the atmospheric state. For the data selection, we use a cutoff value of $\eta = 0.8$. This value was determined by numerical experimentation by gradually decreasing η and choosing the smallest value at which no noticeable degradation of the verification statistics was observed.

5. Results

a. Analysis and forecast verification results

We find a reduction in the horizontally averaged analyses and forecast error statistics that is statistically significant at the 99% level, as a result of adding the satellite radiance observations to the assimilated data set, only in the SH extratropics (Fig. 3). The assimilation of the radiance observations with the proposed strategy improves the analysis and forecast not only of the temperature, which is the model variable most closely related to the radiance through the observation operator, but also of the two horizontal components of the wind. This result suggests that the ensemble-based estimate of the cross-correlation between the errors in the background temperature and wind is sufficiently accurate to lead to an improvement of the wind analysis. Figure 3 also shows that the bias correction has a positive effect on the quality of the analyses and forecasts. This positive effect is especially large in and above the upper troposphere, where the assimilation of the AMSU-A observations without bias correction degrades the analysis and forecast of the temperature and the geopotential height.

Further details of the analysis and forecast improvement patterns are revealed by the vertical cross-sections of the reduction in the zonal mean of the analysis and forecast errors (Figs. 4). The primary region of analysis improvement is in the SH midlatitudes, while a smaller secondary region is the NH polar region. In these two regions, both the temperature and the wind analyses are improved. On the other hand, the temperature analysis in the SH polar region and the wind analysis between 45°S and 75°N are degraded. The magnitude of the improvement, especially for the wind, is much larger than that of the degradation. The

improvement in the SH midlatitudes is also present in the 48-h forecasts, but the improvements in the NH polar region and the degradation in the wind in the Tropics are not present in the 48-h forecasts.

The difference between the analysis and short-term forecast verification results suggests that the analysis verification results may be contaminated by errors in the verifying analyses. For instance, a stronger correlation between the errors in the analyses with satellite radiance observations and the errors in the verifying analyses may lead to the spurious detection of analysis improvement. Likewise, a stronger correlation between the errors in the analyses without the satellite radiance observations and the errors in the verifying analyses could lead to the false detection of analysis degradation. It is also possible, of course, that changes in the quality of the state estimates disappear from the forecasts due to the short predictability limit of the atmospheric flow features that are analyzed with different accuracy in the two analyses that serve as initial conditions of the two verified forecasts.

We cannot tell which one of these potential explanations applies to our results. Nevertheless, we can conclude with high confidence that the assimilation of radiance observations with our proposed strategy is a source of analysis improvement that leads to significant forecast improvement in the SH midlatitudes.

The horizontal distribution of the improvement in the 48-h forecasts is shown in Figs. 5 and 6. The only difference between these two figures is that, in Fig. 6, the difference between the forecast errors is not shown at locations where it is not statistically significant at the 90% level. (We include the figure showing unfiltered results to illustrate the effect of filtering based on statistical significance). This pair of figures indicates that the analyses are improved over the oceans, with the largest improvement between and east of Cape Horn and

the Antarctic Peninsula, while the analyses are degraded over Antarctica. The statistically significant improvement in the surface pressure forecasts indicates that the ensemble-based estimate of the background error covariance matrix provides useful information about the cross correlation between the surface pressure and the atmospheric state variables that directly affect the radiative transfer.

b. The behavior of the bias parameters

These last results demonstrate that the tested strategy provides stable estimates of the state and the bias parameters. Figures 7 and 8 show the time evolution of the error in the temperature and the meridional wind component analyses: in particular, after a short period (about 10 days) of transient behavior, the errors oscillate around relatively stable levels. Furthermore, in agreement with Fig. 3, the results indicate that the bias correction has a larger positive effect in the upper troposphere than in the lower troposphere and that employing a bias correction scheme is especially important for the temperature analysis to benefit from the AMSU-A observations.

To illustrate the behavior of the bias correction terms, we choose two channels: one that has the average peak sensitivity in the lower troposphere (channel 4) and one that is most sensitive, on average, to the atmospheric conditions in the upper troposphere (channel 11). (See Table 1 for the levels of average peak sensitivity for the different channels.) We investigate the time evolution of the bias correction terms for these two channels in the extratropical SH region. The estimate of the total bias, b_j, for the two selected channels, settles after an about 3–4 week transient period (Fig. 9). Once the transient damps out, the

root-mean-square of b_j is about 0.9 K for channel 4 and about 0.3 K for channel 11. That the root-mean-square of the bias correction is larger than its absolute value for both channels indicates that there is a noticeable variability in the magnitude of the bias correction over the different locations.

Figure 10 decomposes the total bias correction into three components: intercept (β_j^0), scan angle ($\beta_j^1 p_1$), and surface temperature ($\beta_j^2 p_2$). Since the root-mean-square and the absolute value of the mean is about the same for the intercept and the surface temperature components, the spatial variability of b_j is primarily due to the variation in the scan-angle term. The magnitude of all three bias correction components is larger for channel 4 than the magnitude of the respective components for channel 11. The two largest magnitude components, which are the intercept and the surface temperature components for both channels, have opposite signs, with the intercept having somewhat larger magnitude.

Finally, Fig. 11 shows the areal mean of the ensemble mean and the ensemble spread of the estimates of the bias parameters β_j^0, β_j^1, and β_j^2. The ensemble spread converges rapidly for channel 4 but slowly for channel 11. For the latter channel, there are three clearly distinguishable phases in the evolution of the estimates of the bias parameters β_j^0 and β_j^2: an initial rapid drift, an oscillatory phase around a well-determined mean level, and a phase in which the oscillations disappear. The beginning of this final phase coincides with the time at which the ensemble spread reaches its asymptotic value. That the estimates oscillate around the final levels in the oscillatory phase suggests that the low asymptotic level of the spread may not necessarily be the sign of a pathological collapse of the ensemble but instead may indicate low uncertainty in the bias parameters for channel 11. Support for this conclusion comes from the fact that channel 11 has average peak sensitivity at a pressure level (280 hPa)

where the bias correction has a large positive effect on the accuracy of the analysis.

6. Conclusions

In this paper, we test the techniques developed by Fertig et al. (2007, 2009) for the assimilation of satellite radiance observations in a realistic setting for the first time. The results suggest that the tested strategy can extract useful information about the atmospheric state, especially in regions where the satellite radiance observations are the dominant source of observational information.

Our approach for bias correction, which is based on a simultaneous estimation of the state and bias parameters based on an ensemble, is not the only way to estimate and to correct for the bias in the radiance observations in an ensemble-based data assimilation system. Fertig et al. (2009) also introduced, in addition to the algorithm tested here, a two-step approach in which the bias correction parameters first are estimated with the ensemble-based scheme and then the state is estimated in a subsequent step. We have recently learned of another alternative strategy proposed by Miyoshi and Whitaker (2009): a single estimate of each bias parameter is obtained, instead of the ensemble of bias parameters in the two schemes by (Fertig et al. 2009), by solving an algebraic equation. Preliminary results with an implementation of the scheme of (Miyoshi and Whitaker 2009) on the model component of the NCEP GFS suggest that the scheme can efficiently account for the observation bias (Jeffrey Whitaker, personal communication). While a comparison of the different approaches for observation bias correction in ensemble-based data assimilation systems would be desirable, the results so far suggest that efficient online estimation and correction of the observation

bias in an ensemble-based scheme for a realistic setting is attainable.

Acknowledgments.

The work of J. A. on this project was partially funded by the Conselho Nacional de Desenvolvimento Cientfico e Tecnolgico (CNPq, National Council for Scientific and Technological Development of Brazil) under the grants PDE 201185/2005-9 and PU 484245/2006-6. Further funding for the research we report here was provided by NASA (Grants NNX08AD40G, NNX07AV45G, and NNX08AD37G) and NSF (Grant ATM0722721).

REFERENCES

Bonavita, M., L. Torrisi, and F. Marcucci, 2008: The ensemble kalman filter in an operational regional nwp system: Preliminary results with real observations. *Quart. J. Roy. Meteor. Soc.*, **134**, 1733–1744.

Burgers, G., J. P. van Leeuwen, and G. Evensen, 1998: Analysis scheme in the ensemble kalman filter. *Mon. Wea. Rev.*, **126**, 1719–1724.

Dee, D. P., 2005: Bias and data assimilation. *QJRMS*, **131**, 3323–3343.

Derber, J. C. and W.-S. Wu, 1998: The use of tovs cloud-cleared radiances in the ncep ssi analysis system. *Mon. Wea. Rev.*, **126**, 2287–2299.

Evensen, G., 1994: Sequential data assimilation with a nonlinear quasi-geostrophic model using monte carlo methods to forecast error statistics. *J. Geophys. Res.*

Eyre, J. R., 1992: A bias correction scheme for simulated tovs brightness temperatures. Tech. Rep. 186, 28pp., ECMWF Tech. Memo, European Centre for Medium-Range Weather Forecasts, Shinfield Park, Reading, Berkshire R62 9AX, United Kingdom.

Fertig, E. J., B. R. Hunt, E. Ott, and I. Szunyogh, 2007: Assimilating non-local observations with a local ensemble kalman filter. *Tellus*, **59A**, 719–730.

Fertig, E. J., et al., 2009: Observation bias correction with an ensemble kalman filter. *Tellus*, **61A**, 210–226.

Friedland, B., 1969: Treatment of bias in recursive filtering. *IEEE Trans. Auto. Control*, **14**, 359–367.

Han, Y., P. van Delst, Q. Liu, F. Weng, and J. C. Derber, 2005: User's guide to the jcsda community radiative transfer model (beta version). Tech. rep., Joint Center for Satellite Data Assimilation, Camp Springs, MD, USA.

Harris, B. A. and G. Kelly, 2001: A satellite radiance-bias correction scheme for data assimilation. *QJMS*, **127**, 1453–1468.

Houtekamer, P. L. and H. L. Mitchell, 1998: Data assimilation using an ensemble kalman filter technique. *Mon. Wea. Rev.*, **126**, 796–811.

Houtekamer, P. L., H. L. Mitchell, G. Pellerin, M. Buehner, M. Charron, L. Spacek, and M. Hansen, 2005: Atmospheric data assimilation with an ensemble kalman filter: Results with real observations. *Mon. Wea. Rev.*, **133**, 604–620.

Hunt, B. R., E. J. Kostelich, and I. Szunyogh, 2007: Efficient data assimilation for spatiotemporal chaos: A local ensemble transform kalman filter. *Physica D*, **230**, 112–126.

Hunt, B. R., et al., 2004: Four-dimensional ensemble kalman filtering. *Tellus*, **56A**, 273–277.

Miyoshi, T. and Y. Sato, 2007: Assimilating satellite radiances with a local ensemble transform kalman filter (letkf) applied to the jma global model (gsm). *SOLA*, **135**, 37–40.

Miyoshi, T. and J. S. Whitaker, 2009: An adaptive bias correction method for satellite data in ensemble kalman filter. *to be submitted*.

Miyoshi, T. and S. Yamane, 2007: Local ensemble transform kalman filtering with an agcm at a t159/l48 resolution. *Mon. Wea. Rev.*, **135**, 3841–3860.

Olsen, E. T., 2007: Airs/amsu/hsb version 5 data disclaimer. Goddard Space Flight Center, NASA, Jet Propulsion Laboratory, California Institute of Technology, Pasadena, CA, [Available online at `http://disc.gsfc.nasa.gov/AIRS/documentation/v5_docs/AIRS_V5_Release_User_Docs/V5_Data_Disclaimer.pdf`], [Available online at `http://disc.gsfc.nasa.gov/AIRS/documentation/v5_docs/AIRS_V5_Release_User_Docs/V5_Data_Disclaimer.pdf`].

Ott, E., et al., 2004: A local ensemble kalman filter for atmospheric data assimilation. *Tellus*, **56A**, 415–428.

Szunyogh, I., E. J. Kostelich, G. Gyarmati, E. Kalnay, B. R. Hunt, E. Ott, E. Satterfield, and J. A. Yorke, 2008: A local ensemble transform kalman filter data assimilation system for the ncep global model. *Tellus*, **60A**, 113–130.

Szunyogh, I., E. J. Kostelich, G. Gyarmati, D. J. Patil, B. R. Hunt, E. Kalnay, E. Ott, and J. A. Yorke, 2005: Assessing a local ensemble kalman filter: perfect model experiments with the national centers for environmental prediction global model. *Tellus*, **57A**, 528–545.

Torn, R. D. and G. J. Hakim, 2008: Performance characteristics of a pseudo-operational ensemble kalman filter. *Mon. Wea. Rev.*, **136**, 3497–3963.

Whitaker, J. S., G. P. Compo, X. Wei, and T. M. Hamill, 2004: Reanalysis without radiosondes using ensemble data assimilation. *Mon. Wea. Rev.*, **132**, 1190–1200.

Whitaker, J. S., T. M. Hamill, X. Wei, Y. Song, and Z. Toth, 2008: Ensemble data assimilation with the ncep global forecast system. *Mon. Wea. Rev.*, **136**, 463–482.

Wilks, D. S., 2006: *Statistical Methods in the Atmospheric Sciences.* 2d ed., Academic Press, 627 pp.

Wu, W.-S., J. R. Purser, and D. F. Parrish, 2002: Three-dimensional variational analysis with spatially inhomogeneous covariances. *Mon. Wea. Rev.*, **130**, 2905–2916.

List of Figures

FIG. 1. Spatial distribution of the conventional temperature observations in a typical 6-hour observation time window. The locations of the observations that were assimilated at grid points between sigma levels 0.45 and 0.55, at February 15, 2004, 1200 UTC are marked by crosses. The total number of observation locations in this figure is 1415.

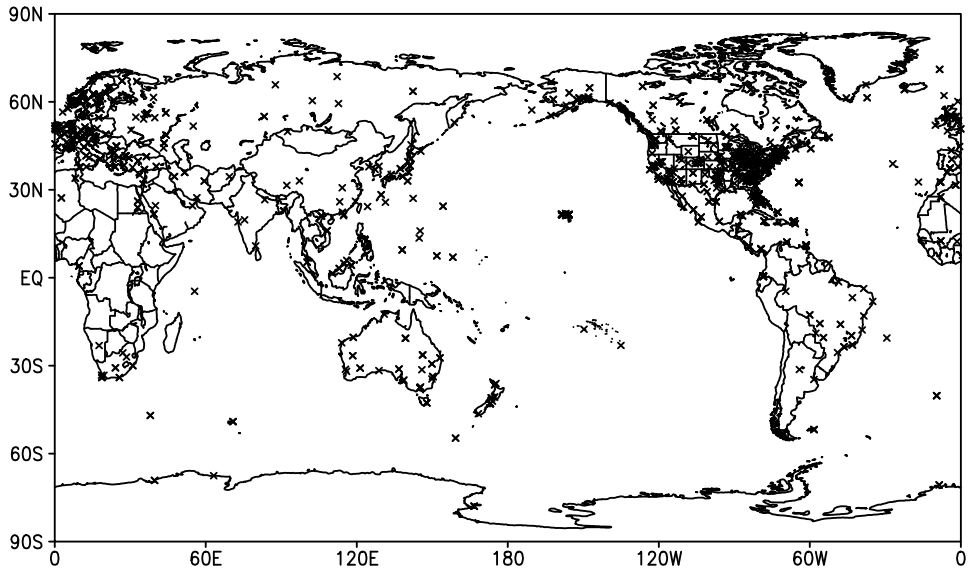

FIG. 2. Spatial distribution of the AMSU-A observations in a typical six-hour observation time window. The locations of the observations that were assimilated at February 15, 2004, 1200 UTC are marked by crosses. The total number of observation locations in this figure is 6394.

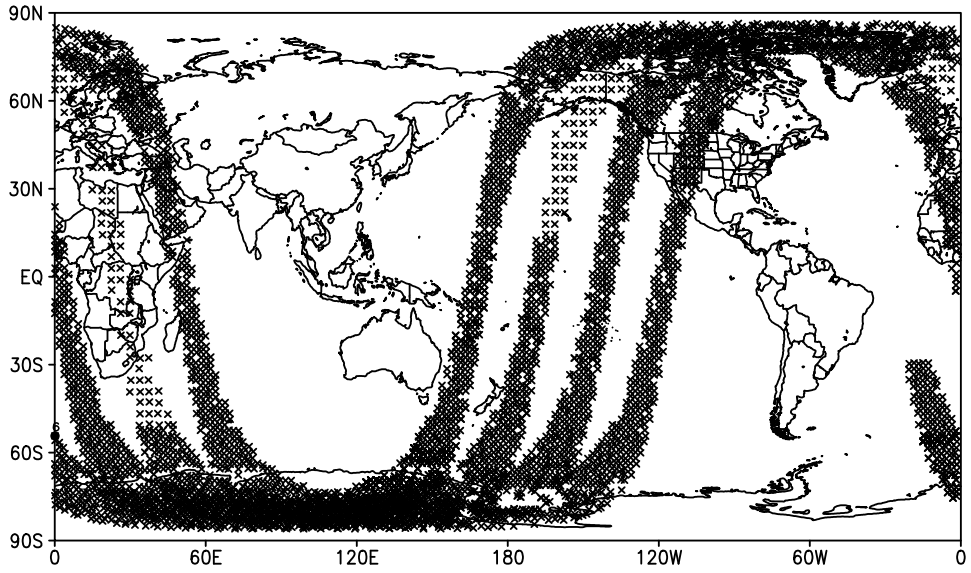

FIG. 3. The left panels show the time mean of the root-mean-square error of the analyses with the satellite radiance observations using bias correction (blue), with the satellite radiance observations not using bias correction (green) and without satellite radiance observations (red) for different forecast variables in the SH extratropics. Right panels show the time mean of the root-mean-square error of the 48-hour forecasts. In the computation of the root-mean-square error, the operational NCEP analysis is used as proxy for the true state of the atmosphere. The averages are taken over all model grid points south of 20°N and over all verification times between 10 January 2004 0000UTC and 29 February 2004 1800UTC for the analysis and between 12 January 2004 0000UTC and 29 February 2004 1800UTC for the forecasts.

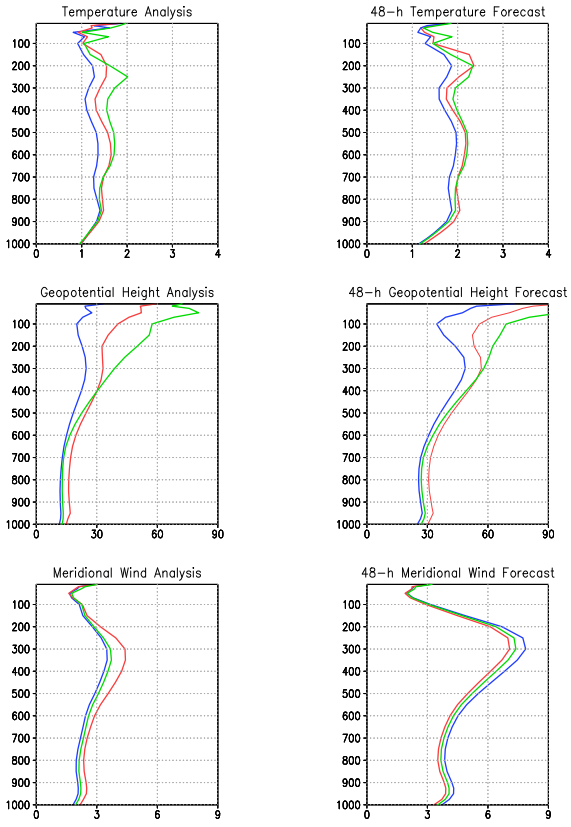

FIG. 4. Vertical cross-section of the difference between the zonal mean absolute error in the state estimate with satellite radiance observations and the zonal mean absolute error in the state estimate without satellite radiance observations. (Negative values indicate improvements due to the assimilation of the satellite radiance observations.) Results are shown for the temperature (top panels) and the meridional component of the wind. The averages are taken over all model grid points south of 20°N and over all analyses times between 11 January 2004 0000UTC and 29 February 2004 1800UTC.

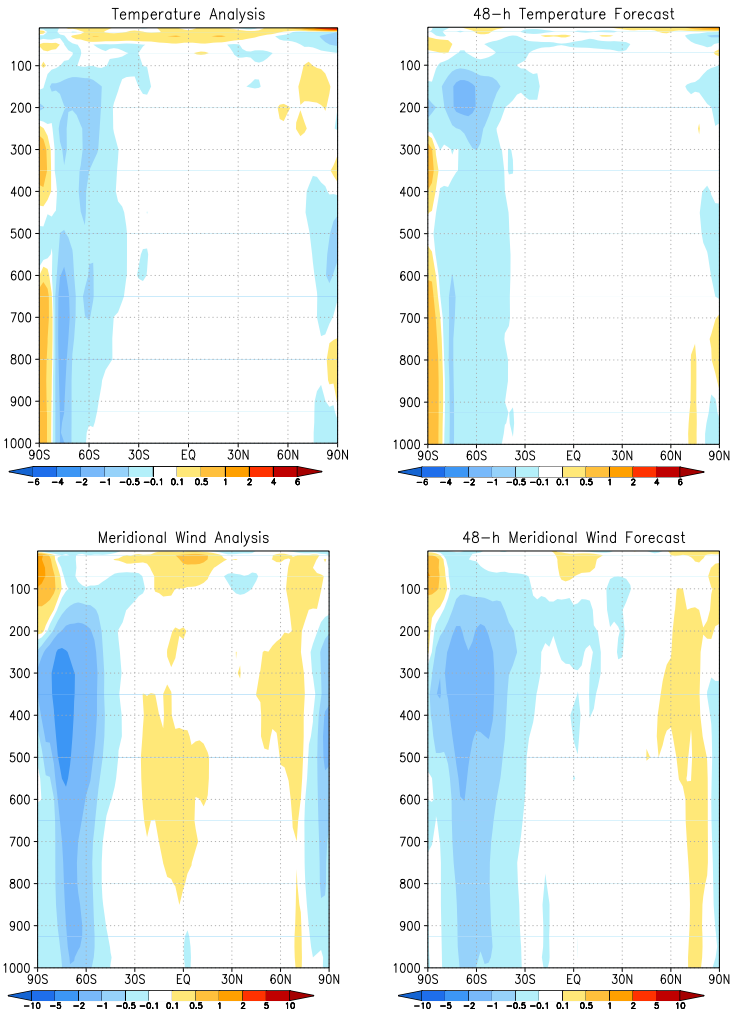

FIG. 5. Color shades show the difference between the mean-square error of the 48-hour forecasts with and without satellite radiance observations. (Negative values indicate regions where the error is reduced by the assimilation of the satellite radiance observations.) The average is taken over all forecasts started between 11 January 2004 0000UTC and 27 February 2004 1800UTC. Contours show the time means of the verifying analysis.

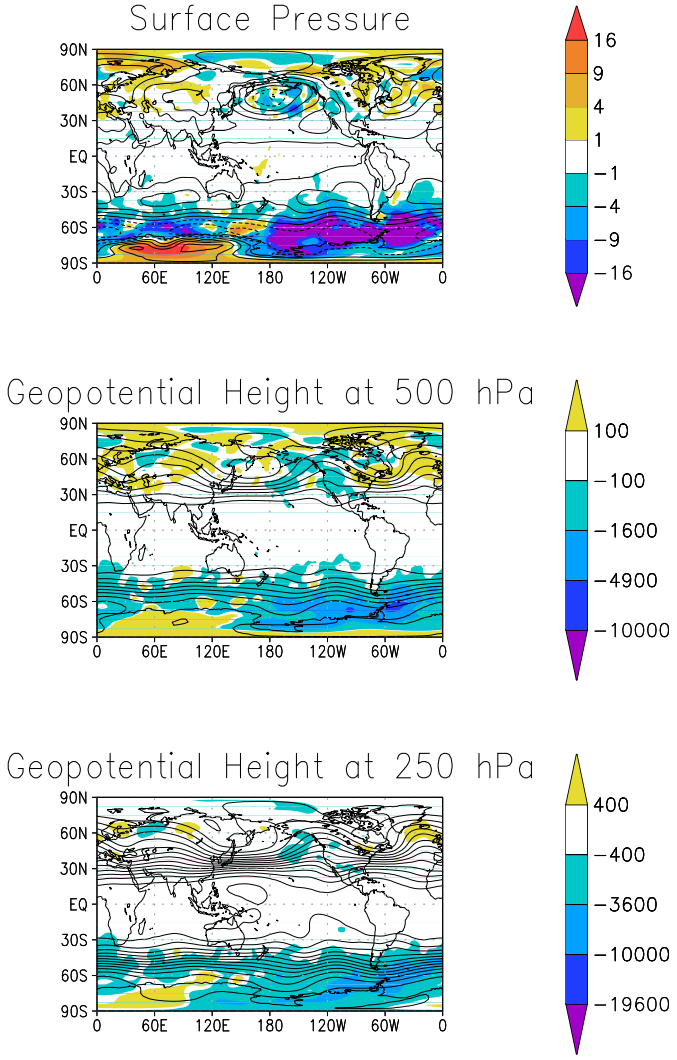

FIG. 6. Same as Fig. 5, except that the difference between the errors in the two forecasts is shown only at locations where it is significant at the 90% level.

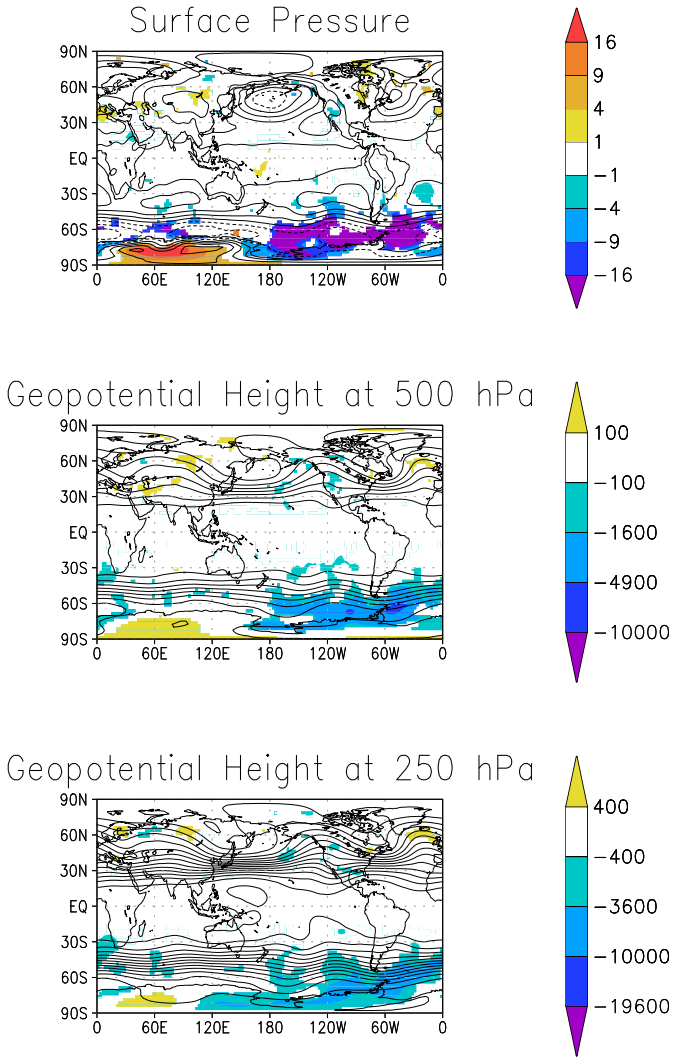

FIG. 7. Time evolution of the root-mean-square error in the temperature analysis at three different model levels in the SH. Shown are the results with the satellite radiance observations using bias correction (blue), with the satellite radiance observations not using bias correction (green) and without satellite radiance observations (red).

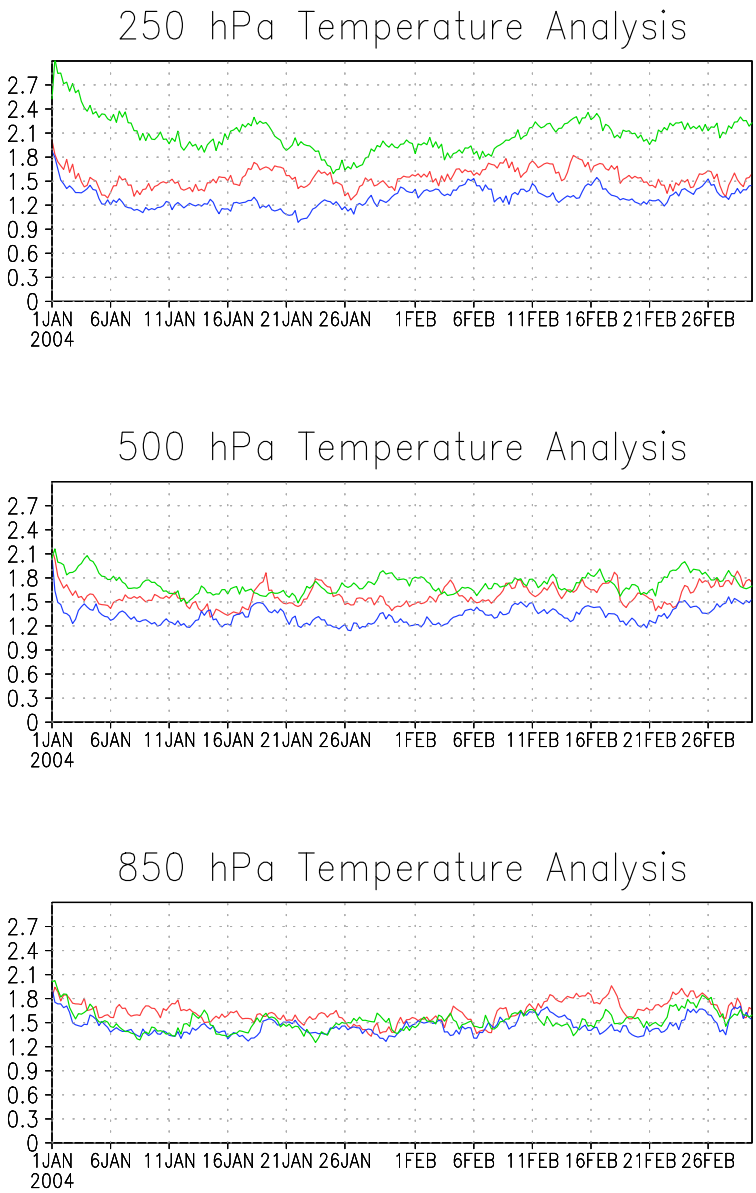

FIG. 8. Same as Fig. 7 except for the meridional component of the wind instead of the temperature.

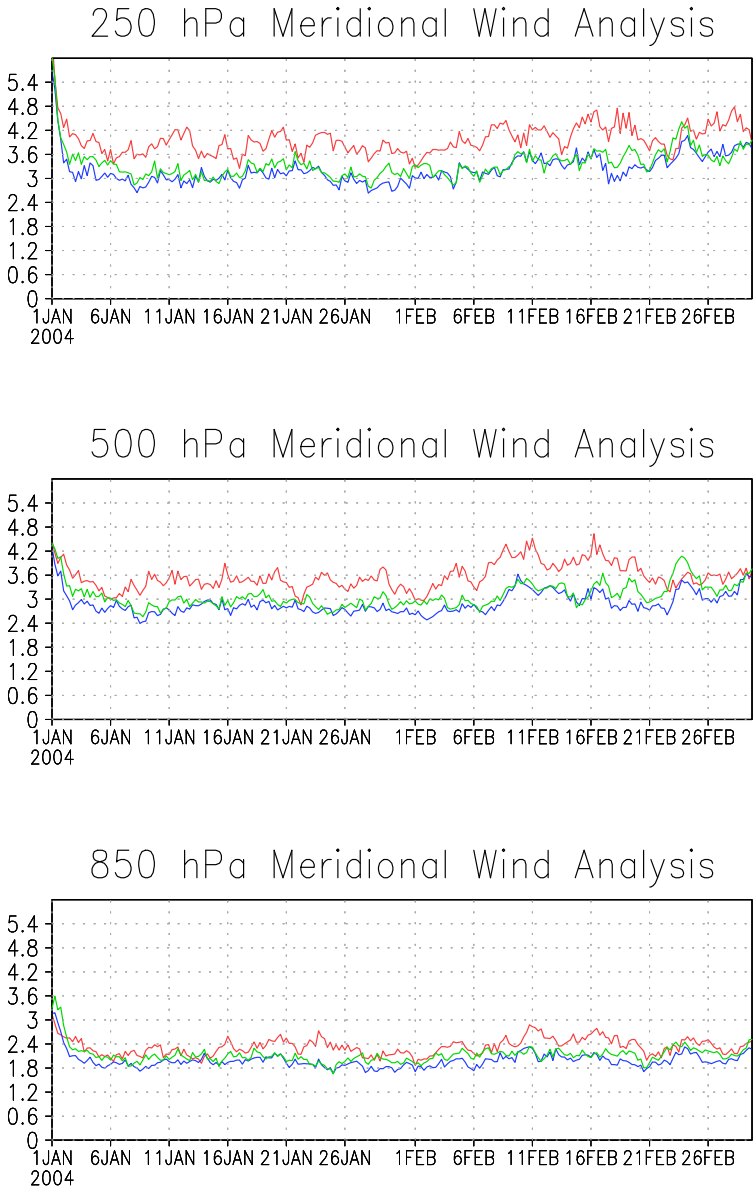

FIG. 9. Time evolution of the areal mean (thick solid line) and the root-mean-square (thin dashed line) of the ensemble mean bias correction for channel 4 (top panel) and channel 11 (bottom panel) in the SH region.

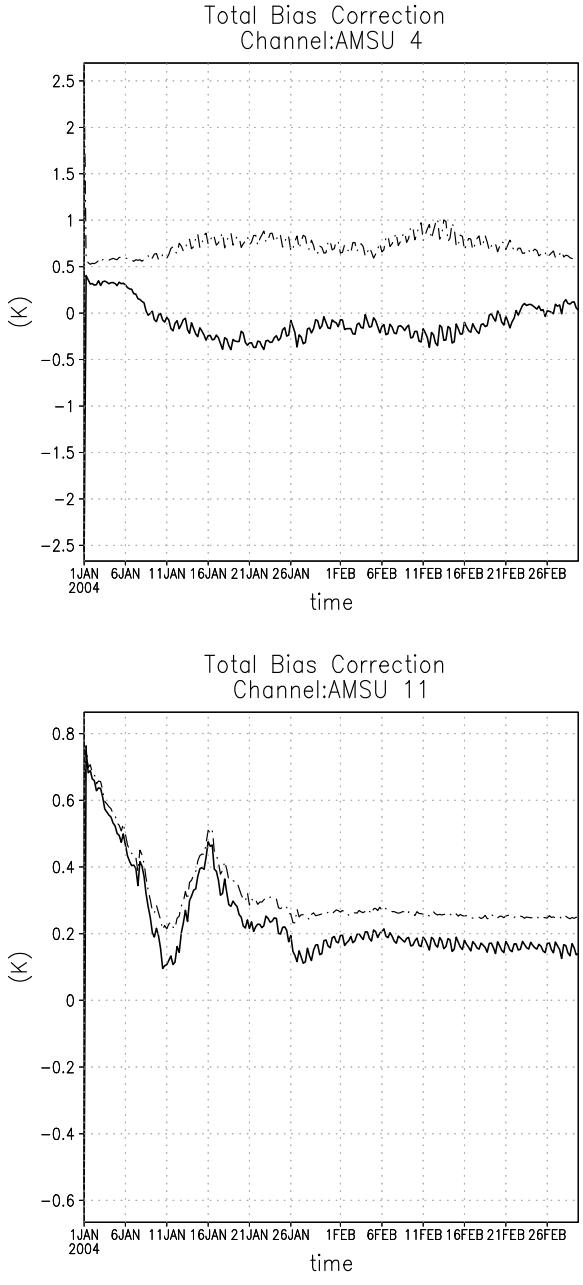

FIG. 10. Time evolution of the areal mean (thick solid line) and the root-mean-square (thin dashed line) of the ensemble mean bias correction components for channel 4 (left panels) and channel 11 (right pannels) in the SH region.

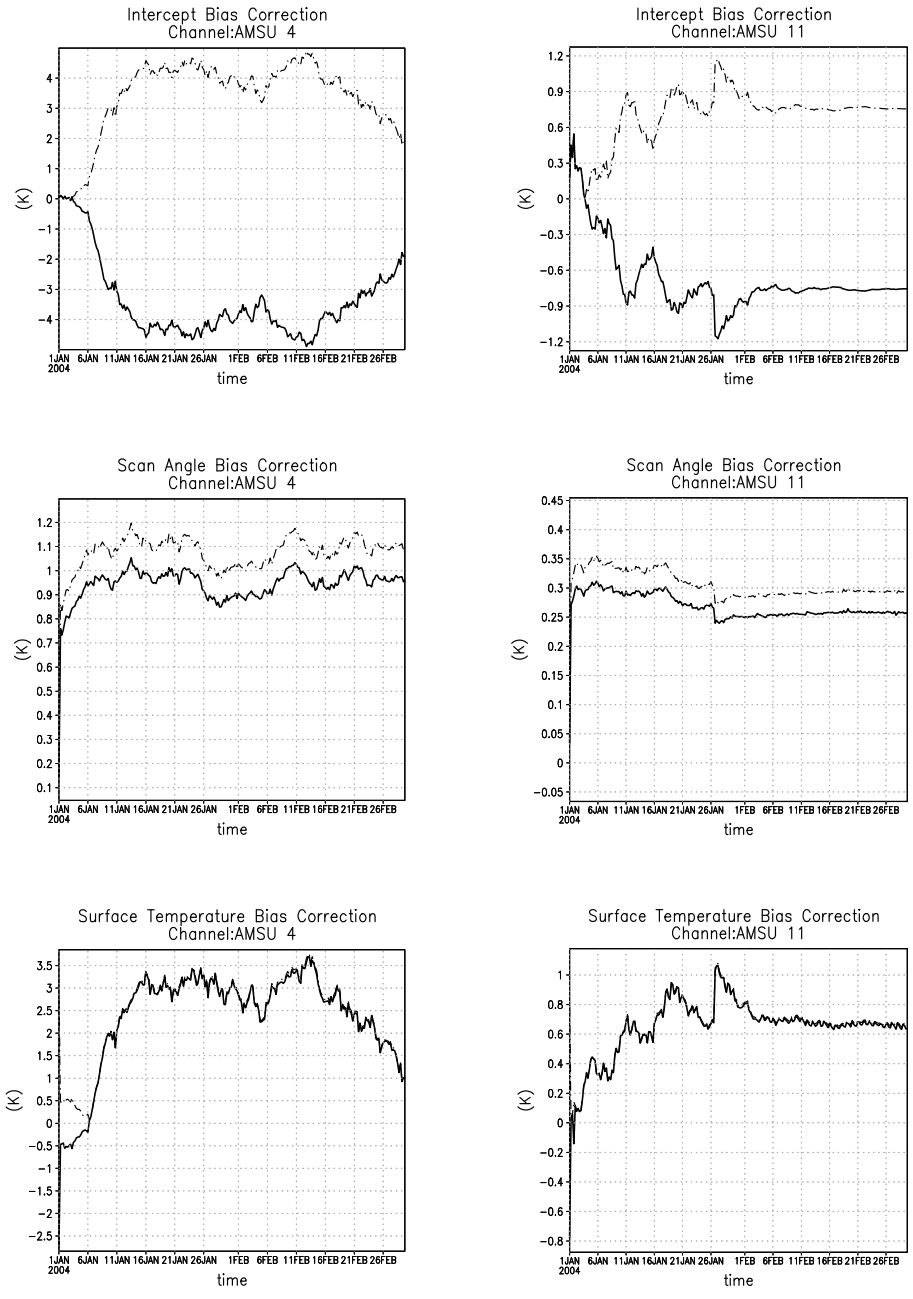

FIG. 11. Time evolution of the bias correction parameters for channel 4 (left panels) and channel 11 (right panels) in the SH region (thick solid line). Also shown is the time evolution of the ensemble spread, defined by the standard deviation, of the estimates of the bias parameters (thin dashed line).

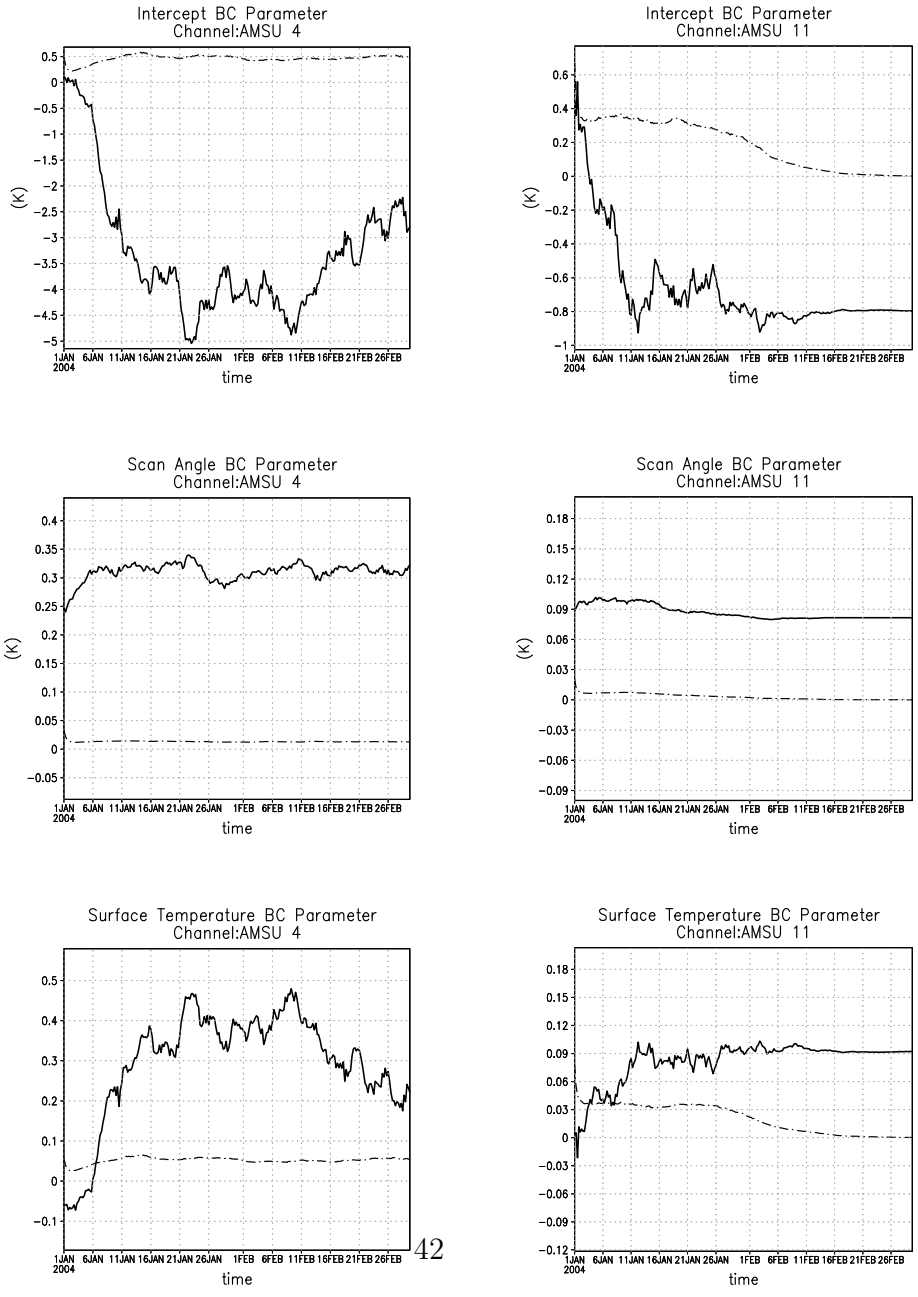

List of Tables

TABLE 1. AMSU-A channels selected for assimilation.

AMSU Channel Number	Average peak of WF (hPa)
4	850
5	700
6	600
7	500
8	400
9	350
10	300
11	280

TABLE 2. Number of assimilated observations on a typical day (January 31, 2004).

Assimilation Cycle	0000 UTC	0600 UTC	1200 UTC	1800 UTC	Daily total
AMSU-A	34,694	35,131	35,794	36,133	141,752
Pressure	12,214	11,413	12,272	11,235	47,134
Temperature	44,424	17,325	39,385	26,060	127,194
Zonal Wind	97,531	64,622	93,899	77,322	333,374
Meridional Wind	97,948	64,911	94,256	77,373	334,488
Total	286,811	193,402	275,606	228,123	983,942